PHYSICAL REVIEW B VOLUME 22, NUMBER 10 15 NOVEMBER 1980

Phase transition and shock-compression parameters to 120 GPa for three types of graphite and for amorphous carbon

W. H. Gust
University of California, Lawrence Livermore National Laboratory, Livermore, California 94550
(Received 2 July 1980)

Shock-induced graphite-to-diamond phase transition pressures and Hugoniot parameters to 120 GPa are presented for pyrolytic, Ceylon natural, and synthetic graphites. The response of amorphous carbon to shock loading, including a shock-induced phase transition, is reported. Interpretations of discontinuities found in the shock-velocity versus particle-velocity plots are discussed in terms of the carbon phase diagram. Evidence of a solid-to-solid phase transition from diamond to a metallic state at very high pressure is described.

I. INTRODUCTION

The study of shock-induced density modifications of carbon is of interest because reliable measurements may be made at considerably higher pressure[1] than before. In 1961 DeCarli and Jamieson[2] found that samples of spectroscopically pure artificial graphite recovered after exposure to explosively driven shocks (~ 30 GPa for about 1 μs) contained particles indicating that some of the material had transformed to the diamond phase. Because they were unable to detect diamond in similar experiments using pure hexagonal graphite, they proposed that the mechanism for the shock-induced transformation was simple compression of the c axis in small rhombohedral domains in the initial crystal structure of the first samples.

A few months later Alder and Christian[3] reported pressure-volume shock data to about 80 GPa for natural Ceylon graphite. Their comparison of the measured free-surface velocities with the corresponding particle velocities (determined through impedance matching) indicated that the transformation was initiated at about 18 GPa and appeared to be driven nearly to completion at 40 to 60 GPA. They also noted a large discontinuity in the P vs V curve above 60 GPa that they interpreted as a transformation from the diamond to a new close-packed liquid state. The transition of diamond to a metallic state is to be expected if carbon exhibits the same behavior under very high compression as the group IV-A homologs, silicon and germanium.[4–7]

In early work, static pressure experimental results by Bundy[8] indicated that an irreversible graphite-to-diamond transition occurred at about 12.5 GPa and 3000 K. Strong[9] and Bundy and Strong[10] reported that the transformation is catalyzed by group VIII metals, manganese and chromium.

Pavlovskii and Drakin[11] published shock-wave data on synthetic graphite ($\rho_0 = 1.85$ Mg/m^3) to 300 GPa. Their results and those of Alder and Christian agreed to 60 GPa, but they found no evidence for a transition to the liquid or metallic state at pressures to 300 GPa. In an effort to eliminate any time dependent effects in the transformation, Trunin *et al.*[12] made similar measurements with 70-mm thick samples of chemically pure graphite that agreed with those of Pavlovskii and Drakin. The Alder and Christian data above 65 GPa are now believed to be in error because of interference by elastic release waves caused by reverberations in the very thin projectile plates they used to obtain the higher pressures.

Doran[13] and Coleburn[14] performed shock experiments to 50 GPa on high-density pyrolytic graphite. In that pressure range, they found no shock compression anomalies that could be related to a transformation to the diamond structure. They also noted that the pressure-versus-volume data for pyrolytic graphite differed significantly from the results for natural Ceylon graphite reported by Alder and Christian[3]; the pyrolytic graphite was less compressible. Doran's inclined mirror experimental system[13] could resolve multiple wave shock structures, but none were seen. Coleburn[14] detected no differences in compressibility characteristics for shocks propagated normal to and parallel to the c axis.

Shock compression data for pyrolytic graphite to 80 GPa by McQueen and Marsh[15] exhibit discontinuities in the U_s vs U_p curves at $U_p \simeq 2.35$ and 3.5 km/s that are probably related to initiation of a transformation, a mixed phase region, and complete transformation to the diamond phase. Their data for several pressed graphites with densities varying from 2.13 to 1.54 Mg/m^3 indicate that the material with the lower initial density has a lower shock velocity for a given driving system. In addition, each of the pressed graphites exhibited a discontinuity in the slope of the U_s vs U_p curve at about $U_p \sim 1.9$ to 2.0 km/s. These

discontinuities are probably related to the initiation of the graphite-to-diamond transition. They also found no difference in the response of pyrolytic graphite to shocks perpendicular or parallel to the c axis.

Using x-ray diffractometry on recovered specimens, Trueb[16] found that shock compression (to 100 GPa) of full density graphite inclusions in an iron matrix produced both cubic and hexagonal diamonds. The production of hexagonal diamonds was attributed to relatively rapid thermal quenching action by the iron matrix. Similar experiments[17] with mechanically compacted mixtures of copper and graphite produced only cubic diamonds.

In electrical resistivity experiments by Bundy[8] and Aust and Drickamer[18] when highly oriented pyrolytic graphite was compressed along the c axis, the behavior was different than for random polycrystalline graphite. Bundy recovered polycrystalline diamonds from samples exposed to pressures of 12.5 GPa at about 3000 K. He did not detect any wurtzite phase in that work.

Bundy and Kasper[19] recovered hexagonal diamonds from highly oriented samples exposed to pressures greater than 13.0 GPa and temperatures exceeding 1300 K. Hanneman, Strong, and Bundy[20] reported that the static catalyst-molten-metal process yields only cubic diamonds. They also stated that formation of cubic diamond from randomly oriented polycrystalline graphite requires threshold temperatures from 3500 K at 13.0 GPa to 2500 K at 23.0 GPa static pressure. Also, diamonds formed by freezing liquid carbon at pressures greater than the graphite-diamond-liquid triple point (13 GPa) are of the cubic type. They also noted that there was no evidence to indicate that cubic diamond could be transformed into hexagonal diamond by applying static or shock pressure. Diamonds from the large iron-nickel Canyon Diablo meteorite consist of randomly oriented hexagonal and cubic crystallites.[20]

Recently Vereshchagin *et al.*[21] reported anomalies in measurements of the electrical resistivity of diamond at about 100 GPa, which they interpret as evidence for a transformation from diamond to a metallic state. On the other hand, Pavlovskii[22] reported that shock compression of diamond to 500 GPa did not cause metallization.

Shock-wave measurements by the inclined prism technique have been refined so that sensitive resolution of multiple shock structures associated with anomalous material behavior can be done. Further, the two-stage light-gas gun[23] has been developed into a dependable source of very high-pressure planar shocks. These improvements present an opportunity to reexamine the low-pressure shock-compression characteristics for graphite, where some disagreement exists, and to extend the data to high-pressure regimes in a search for the transformation to the metallic state.

II. PROCEDURE

Our determination of the equation of state of graphite is based on measurements made on samples exposed to hydrodynamic shocks generated by high explosive systems and, at higher pressure, through use of flying plate impacts from a two-stage light-gas gun. The data from a series of these experiments are used to determine the loci of points describing all possible pressure-volume, energy-volume, and pressure–particle-velocity states achievable through shock compression of the material. These curves, Hugoniots, are obtained through use of the Hugoniot relations, which are derived through the application of the conservation of mass, momentum, and energy across the shock front. For multiple-wave shocks these are

$$V_n = V_{n-1}\frac{U_{s_n} - U_{p_n}}{U_{s_n} - U_{p_{n-1}}} \quad , \tag{1}$$

$$P_n - P_{n-1} = V_{(n-1)}^{-1}(U_{s_n} - U_{p_{n-1}})(U_{p_n} - U_{p_{n-1}}) \quad , \tag{2}$$

$$e_n - e_{n-1} = \tfrac{1}{2}(P_n - P_{n-1})(V_{n-1} - V_n) \quad . \tag{3}$$

Here ρ, V, U_s, U_p, P, and e are density, specific volume ($V = 1/\rho$), shock velocity, particle or mass velocity, pressure or stress, and specific energy. The order of the successive waves is denoted by n. For the stresses obtained here, P_0 is considered negligible compared to P_1.

In this series the inclined prism, flash gap, and electrically biased pin-measurement techniques were applied to three grades of graphite with initial densities varying from 2.22 to 1.70 Mg/m^3 and to a grade of amorphous carbon of initial density 1.54 Mg/m^3. The inclined prism technique was used with explosively driven shock systems, which produced pressures from about 5 to 30 GPa in the graphite, in an attempt to observe possible multiple shock-wave structures that might be related to shock-induced polymorphism. The flash gap techniques was used with explosively driven systems at pressures between about 8.5 and 70 GPa (see Table I), and the electrical shorting pins were used in experiments performed on a two-stage light-gas gun that produced pressures from 44 to 130 GPa in the graphite.

Briefly, the inclined prism technique[6] uses the principle of loss of total internal reflection within back lighted prisms to measure shock transit times and to resolve multiple-wave shock structures. Even on a smooth flat surface the prism contacts the sample at only a few points, so a void of a micrometer or so exists at the sample-prism interface. When the free surface of the shocked samples moves into complete contact with the prism, it results in a drastic change in the index of refraction of the medium outside the prism and, through loss of total internal reflection,

TABLE I. Shock-generating systems. All systems consisted of a 0.3-m diam plane-wave lens with a 0.3-m right cylinder of high explosive 0.15 m long, unless noted otherwise. All attenuator components were flat and parallel within 5 μm.

System	Shock generators[a]	Attenuator and base-plate material	Component thickness (mm)	Pressure in standard material (GPa ± 5%)
A	Pressed TNT	Brass	25.4	6.3
		Lucite	12.7	
		Al (921T)	12.7	
B	Pressed TNT	Brass	25.4	13.7
		Al (921T)	12.7	
C	Pressed TNT	Al (2024)	12.7	21.5
D	PBX 9205 (RDX)	Al (2024)	12.7	37.0
E	PBX 9404 (HMX)	Al (2024)	12.7	38.5
F	Pressed TNT	Air	3.2	48.0
		Monel	4.0	
		Air	25.4	
		Al (2024)	4.8	
G	Pressed TNT	Air	3.2	53.0
		Monel	3.2	
		Air	25.4	
		Al (2024)	4.8	
H	PBX 9205 (RDX)	Same as system *G*	Same as system *G*	68.0
I	PBX 9404 (HMX)	Same as system *G*	Same as system *G*	79.0
J	Two-stage gun	Ta flyer	1.5	200–400

[a]For a complete chemical description of these pressed and plastic-bonded explosives see LLNL Report No. UCRL-51319 (unpublished).

instantly quenches an illuminating beam. The time related sequence of the light-dark events may then be observed through a slit on a streaking camera.

Shock transit times through the samples are measured with prisms placed flat on the base plate and sample surfaces. The inclined portion of the prism allows continuous-streaking camera observation of the advancing free surface during the time of interest. Through observing the changes in the velocity of the free surfaces, U_{FS}, resolution of multiple shock-wave structures is possible. Initially, total internal reflection along the inclined prism is progressively destroyed by the free-surface–prism contact point moving at U_{FS_1}, and later at U_{FS_2}. The change in free-surface velocity occurs when the boundary is overtaken by the second shock that moves at a rate $(U_{s_2} + U_{p_1}) > U_{FS_1}$. Particle velocity is determined through the free-surface approximation $(2U_{p_1} = U_{FS_1})$ and also through impedance matching.[24] A large disparity between the two values may indicate anomalous behavior under shock compression.

For pressures from 30 to 70 GPa, the shock velocities were measured with flash gaps.[24] In this instance, shock transit times are determined from the time displacement on a streaking camera record of intense flashes of light that occur when the shocked materials close small xenon-filled gaps located at the sample-base plate interface and again at the sample free surface. Particle velocities were determined through impedance matching.

In the experiments on the two-stage light-gas gun,[23] 1.5-mm thick Ta plates were impacted on 25.4-mm diam by 3.2-mm thick graphite samples. In the gun a 90-mm diam plastic-nosed piston is propelled down a 11.7-m long hydrogen-filled tube. The soft-nosed piston compresses the hydrogen into a 90-mm diam to 30-mm diam truncated conical volume that has a burst diaphragm located at the small end. The nose of the piston is swaged into the cone, compressing the hydrogen, and the resulting high gas pressure ruptures the burst diaphragm, thus allowing the hydrogen to expand into an evacuated 29-mm diam × 7.6-m long tube. This expanding gas accelerates a Ta plate bonded to a plastic sabot that was placed initially slightly downstream from the burst diaphragm.

Various projectile velocities were obtained by varying the initial combination of gun powder and static hydrogen pressure; Ta projectile velocities from 3.6 to 6.8 km/s were used here. Particle velocities were determined by impedance matching with the Ta

Hugoniot.[24,25]

For some experiments it was assumed that the material was largely transformed to diamond. In diamond, the bulk sound speed at 1 atm is 11.2 km/s.[26] Consequently it is essential that the geometry for the very high-pressure shots be designed to exlcude "catch-up" waves from reverberations within the impactor as well as edge effects from lateral unloading waves (both are propagating in a compressed diamondlike material).

The geometry used is shown in Fig. 1. Six foil switches were bonded radially on the sample at 60° intervals; they were made of 5-μm thick Manganin[27] foil enclosed in 12-μm thick Mylar and were biased at 150 V. Total thickness for each foil switch was about 30 μm. A 0.8-mm thick shim of Ta protected the foil switches from possible damage by hot gases prior to projectile impact. No corrections were made for uncertainties in the closure time of the foil switches. The foil may have shorted to the protective Ta shim rather than the graphite sample. This introduces an uncertainty of about 2 ns or less than 1%.

The graphite samples were 25.4-mm diam by 3.2-mm thick. On the back side of each sample, six coaxial self-shorting pins were placed in contact so that each was directly in line with a foil switch. The pin array diameter was 12.9 mm. A seventh pin was located at the center of the array. A foil switch and pin paired on the same longitudinal line reduces errors caused by impactor tilt.

The shocks generated by projectile impact shorted the biased foil switches and pins; the resulting pulses were recorded on 10 oscilloscopes arranged in 5 master-slave systems. Two separate measurements were made on each pulse. Oscilloscope sweep nonlinearity was accounted for by interpolating with an accurately known sine wave (10 ns/cycle) placed on each shot record. Shock transit times were corrected for differences in transmission cable lengths and pin closure times. The cable transit time differences

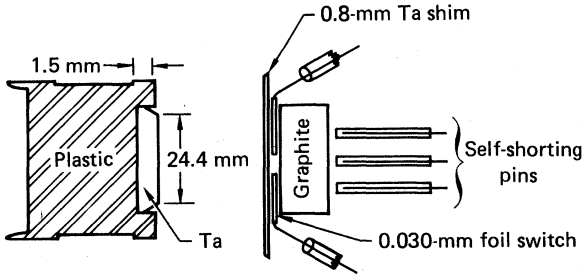

FIG. 1. Schematic of projectile and target. The Ta shim, graphite sample, and outer conductors were at ground potential. The Manganin foils and pin center conductors were biased to 120 V.

were measured with pulse-echo techniques. The pin end-wall and gap thicknesses were determined from x-ray photographs; the brass-shock and free-surface velocity corrections were obtained from an impedance-match solution of the graphite-brass interface for the conditions of each experiment. The x-ray photographs yielded thicknesses that were accurate within 13 μm. For the brass-shock and free-surface velocities used here ($U_s \approx 7$ to 8 km/s, $U_{FS} \approx 6$ to 7 km/s), time uncertainty is about 3 to 4 ns or 1.0 to 1.3% of the transit time through the sample. Total uncertainty for the measurements was less than 2%.

This geometrical arrangement effectively eliminated error caused by "catch-up" and lateral unloading waves. The time-versus-distance plot (Fig. 2) demonstrates the analysis involved for "catch-up" waves.

The edge rarefaction wave propagates laterally through the sample at velocity $\vec{C}_* + \vec{U}_p > \vec{U}_s$, where $\vec{C}_*$ is the sound speed in compressed diamond. As this wave propagates, it overtakes and degrades the shock advancing at U_s. The direction of $\vec{C}_* + \vec{U}_p$ is

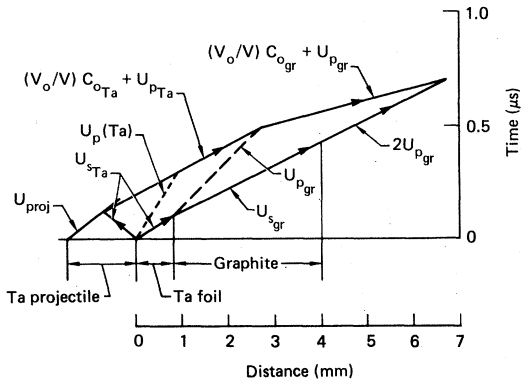

	Material, Ta	Ceylon graphite (gr)
U_s (km/s)	7.12	10.2
U_p (km/s)	3.10	4.90
$(V_o/V)\,C_o + U_p$ (km/s)	9.0	19.5

FIG. 2. Time vs distance diagram comparing the arrival times of the main shock at the sample free surface and of the rarefaction wave from the back side of the Ta flyer plate (data set for $U_p = 4.5$ km/s in Ceylon graphite). The rarefaction wave does not overtake the main shock during the time of the measurement.

obtained from[28]

$$\tan\alpha = \left[\frac{C_*^2 - (U_s - U_p)^2}{U_s^2}\right]^{1/2}, \quad (4)$$

where α is the angle between $\vec{U}_s$ and the resultant of $\vec{C}_* + \vec{U}_p$. The lateral penetration is then simply $1 = H \tan\alpha$ where H is sample thickness. Placing the shorting pins on a 12.7-mm diam effectively eliminated the edge rarefaction waves from the measurements.

III. MATERIALS

The four groups of samples used in these experiments were obtained commercially. The specimens were 50.8 mm × 25.4 mm × 3.2 mm slabs for the inclined prism experiments, 19.0-mm diam × 6.4- or 3.2-mm disks for the flash gap experiments and 25.4-mm diam × 3.2-mm thick disks for the gun experiments. The initial densities of the goups varied from 2.22 to 1.54 Mg/m^3. This variation introduced a substantial difference in temperature along the Hugoniots for the four groups.

Pyrolytic graphite samples were obtained from the Super-Temp Company, Sante Fe Springs, California. Initial densities were about 2.22 Mg/m^3. Debye-Scherer patterns[29] indicated a strong orientation of the c axis normal to the major surfaces (parallel to the shock propagation direction) and a lack of order for other major axes. No significant amount of impurities was detected by x-ray fluorescence analysis.

We were unable to obtain Ceylon graphite samples of uniform density for inclined prism experiments. The samples required for inclined prism experiments were too large for our cold pressing process to manufacture. Disks of Ceylon natural graphite were obtained by cold pressing graphite powder obtained from the Asbury Graphite Mills, Asbury, New Jersey through the kind assistance of E. V. Melder of the Embassy of Sri Lanka. The powder, grade number 518, is a natural Ceylon amorphous lump graphite ground to a fineness of 2% maximum plus 100 mesh and 70 to 85% minus a 200 mesh. Sample densities of about 2.14 Mg/m^3 were obtained by cold pressing to approximately 435 MPa.

Spectrochemical analyses of impurities in the powder indicated there was 0.3, 0.5, and 0.25 at.% Si, Zr, and Fe, respectively; from 0.05 to 0.015 at.% each of Ca, Al, Mg, Cu, and Ti; and less than 0.005 at.% each of Mn, Ni, Mo, Cr, Sr, B, Ba, Ag, and Co. Analysis of a pressed sample by x-ray fluorescence indicated 0.27, 0.42, and 0.1 at.% of S, Fe, and Ca and 0.02 and 0.01 at.% of K and Cu, respectively. Less than 0.005 at.% of Cr, Rb, Sr, Y, Zr, No, and Pb were found. The data indicated that the impurity content varied considerably from sample to sample.

Analyses of the pressed samples by x-ray diffraction[29] showed a strong orientation such that the c axis coincided with the pressing axis (also the direction of shock propagation). Two discrete crystallites of FeS_2 were detected.

The hot pressed synthetic graphite samples were machined from laboratory stock of UCAR-ATJ, molded graphite produced by the Union Carbide Company, Cleveland, Ohio. X-ray fluorescence analysis[29] disclosed about 0.2 at.% Ca, 0.01 at.% V, and 0.002 at.% Fe. X-ray diffraction patterns[29] indicated that to a first approximation the ATJ samples had a random orientation.

Vitreous carbon samples with densities of about 1.54 Mg/m^3 were obtained from the Beckwith Carbon Corp., Van Nuys, California. Vitreous carbon[30] is a hard homogeneous form that lacks the usual crystallographic order. It resembles glass in structure, fracture characteristics, hardness, and low macroscopic porosity. The densities varied slightly from sample to sample within each group. This caused small scatter among the compression data.

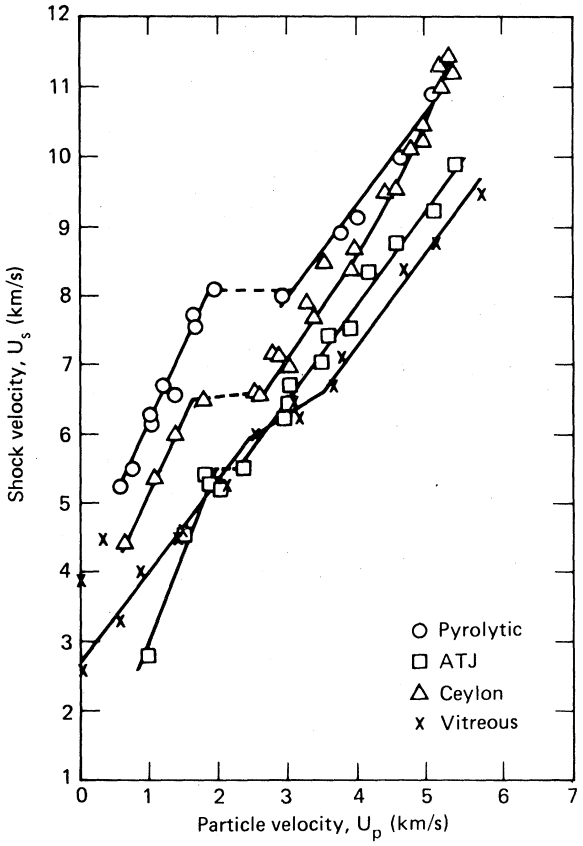

FIG. 3. Shock velocity as a function of particle velocity for shock-compressed pyrolytic, Ceylon natural, and ATJ graphites and for an amorphous form of carbon. Discontinuities at $U_p \approx 1.5$–2.2 km/s mark the onset of transitions to the diamond structure; those at 2.3 to 3.6 km/s mark the completions. The discontinuity in the graph for Ceylon natural graphite at 4.5 km/s appears to be related to an additional transformation.

IV. RESULTS

The data achieved are summarized in Tables II to V. Unpublished flash gap data by Hord[31] are also included in Tables II to V. Discontinuities indicative of anomalous behavior are displayed in Figs. 3 and 4 and the corresponding pressure-versus-volume curve in Fig. 5.

No two-wave shock structures were found for either the pyrolytic or ATJ graphite; the Ceylon graphite samples were not tested for two-wave shock structures. The pyrolytic graphite was shocked parallel to the highly oriented c axis. Excluding the mixed-phase region, the line segments that describe the U_s vs U_p curve (Fig. 3) for the initial and final phases are $U_s = 5.27 + 2.20\ (U_p - 0.6)$ for $0.6 < U_p < 1.9$ km/s and $U_s = 8.11 + 1.33(U_p - 3.1)$ for $3.1 < U_p < 5.2$ km/s. The stresses corresponding to those discontinuities are 34 and 56 GPa.

The plot for Ceylon natural graphite (Fig. 3) exhibited discontinuities at $U_p = 1.65$, 2.55, and 4.55 km/s when shocked parallel to the strongly oriented c axis. The line segments are given by $U_s = 4.26 + 2.17(U_p - 0.6)$ for $0.6 < U_p < 1.65$ km/s, $U_s = 6.67 + 1.50(U_p - 2.55)$ for $2.55 < U_p < 4.55$ km/s, and $U_s = 9.45 + 2.34(U_p - 4.55)$ for $4.55 < U_p < 5.4$ km/s. The stresses corresponding to the discontinuities are 23, 36, and 92 GPA, respectively.

The line segments for partially oriented hot-pressed

TABLE II. Ceylon graphite summary.

Shock system	Base plate: Shock or projectile velocity (km/s)	Base plate: Pressure in standard (GPa)	Base plate: Sound speed at 1 atm (km/s) C_L	Base plate: Sound speed at 1 atm (km/s) C_S	Initial density ρ_0 (Mg/m^3)	Shock velocity U_s (km/s)	Particle velocity U_p (km/s)	Pressure P (GPa)	Volume V (m^3/Mg)
A	5.90[a]	8.5	· · ·	· · ·	2.16	4.38	0.64	6.1	0.395
B	6.46[a]	13.5	· · ·	· · ·	2.19	5.29	1.06	12.3	0.365
C	6.99[a]	22.5	· · ·	· · ·	2.16	6.02	1.37	17.8	0.358
D	7.45[a]	32.2	· · ·	· · ·	2.17	6.52	1.78	25.1	0.336
F	8.32[a]	48.5	· · ·	· · ·	2.18	6.60	2.55	36.7	0.281
F	8.22[b,c]	49.0	1.30	0.97	2.18	6.59	2.58	37.1	0.278
G	8.64[a]	57.8	· · ·	· · ·	2.18	7.16	2.85	44.5	0.276
G	8.64[b]	57.8	1.50	0.97	2.18	7.14	2.88	45.1	0.273
H	9.12[b]	71.2	1.35	0.95	2.18	7.89	3.27	56.2	0.269
H	9.16[a]	73.5	· · ·	· · ·	2.18	7.70	3.41	57.3	0.255
I	9.50[b]	81.6	1.47	1.02	2.18	8.49	3.54	65.5	0.267
J	3.62[d]	96.8	· · ·	· · ·	2.14[e]	6.96	2.98	44.4	0.267
J	6.76[f]	93.2	· · ·	· · ·	2.14[e]	8.39	3.91	70.4	0.250
J	4.95[d]	261	· · ·	· · ·	2.15[e]	8.64	3.97	74.0	0.251
J	5.50[d]	307	· · ·	· · ·	2.15	9.44	4.41	89.5	0.248
J	5.67[d]	323	· · ·	· · ·	2.14[e]	9.47	4.53	92.0	0.243
J	5.99[d]	350	· · ·	· · ·	2.14	10.1	4.77	103	0.247
J	6.16[d]	364	· · ·	· · ·	2.15[e]	10.2	4.90	108	0.242
J	6.22[d]	370	· · ·	· · ·	2.11[e]	10.4	4.94	108	0.249
J	6.64[d]	410	· · ·	· · ·	2.13	11.1	5.22	122	0.249
J	6.71[d]	416	· · ·	· · ·	2.13	11.3	5.25	126	0.251
J	6.84[d]	428	· · ·	· · ·	2.15[e]	11.2	5.38	129	0.245
J	6.84[d]	428	· · ·	· · ·	2.16	11.4	5.33	131	0.245

[a]Shock velocity in 2024 Al standard sample from flash-gap experiments by Hord (Ref. 31).
[b]Shock velocity in 2024 Al standard sample this work.
[c]Flyer plate was 4.0 mm thick.
[d]Ta projectile velocity from light-gas gun experiments.
[e]Samples were isotatically cold pressed. All others for system *J* were cold pressed with dies.
[f]Projectile plate was 2024 Al.

TABLE III. Pyrolytic graphite summary.

High-explosive system	Base plate Shock or free-surface velocity (km/s)	Pressure in standard (GPa)	Sound speed at 1 atm (km/s) C_L	C_s	Initial density ρ_0 (Mg/m^3)	Shock velocity U_s (km/s)	Particle velocity U_p (km/s)	Free-surface velocity U_{FS} (km/s)	Pressure P (GPa)	Volume V (m^3/Mg)	Sound velocity at P C_* (km/s)
A	6.05[a]	8.5	···	···	2.189	5.25	0.59	1.21	6.8	0.405	···
A	1.22[b]	10.5	3.36	0.95	2.223	5.50	0.72	1.41	8.8	0.392	4.98
B	6.53[a]	16.2	···	···	2.193	6.17	1.0	···	13.5	0.383	···
B	6.56[a]	16.3	···	···	2.196	6.24	1.01	···	13.8	0.382	···
C	2.22[b]	21.1	3.37	0.93	2.248	6.70	1.21	2.66	18.3	0.364	6.35
C	6.99[a]	22.5	···	···	2.192	6.61	1.31	2.57	19.0	0.366	···
D	2.97[b]	30.0	3.35	0.95	2.221	7.49	1.60	3.65	26.6	0.355	7.01
D	7.48[a]	31.2	···	···	2.201	7.66	1.64	3.31	27.6	0.356	···
E	3.51[b]	36.5	3.40	0.97	2.223	8.10	1.89	4.16	33.2	0.345	7.53
G	8.85[a]	65.4	···	···	2.206	8.06	3.01	···	53.6	0.284	···
G	8.85[a]	65.4	···	···	2.207	8.06	3.01	···	53.6	0.284	···
I	9.73[a]	88.6	···	···	2.202	8.88	3.70	6.90	72.1	0.265	···
J	4.89[c]	259	···	···	2.223	9.12	3.89	···	79.0	0.258	···
J	5.77[c]	332	···	···	2.223	9.99	4.55	···	101	0.245	···
J	6.60[c]	406	···	···	2.223	10.9	5.17	···	125	0.237	···

[a]Shock velocity from flash-gap experiments by Hord (Ref. 31).
[b]Free-surface velocity from inclined prism experiments.
[c]Ta projectile velocity from light-gas gun experiments.

TABLE IV. Synthetic (ATJ) graphite summary.

Shock system	Base plate Free-surface, shock, or projectile velocity (km/s)	Pressure in standard (GPa)	Sound speed at 1 atm (km/s) C_L	C_s	Initial density ρ_0 (Mg/m^3)	Shock velocity U_s (km/s)	Particle velocity U_p (km/s)	Free-surface velocity U_{FS} (km/s)	Pressure P (GPa)	Volume V (m^3/Mg)	Sound speed at P C_* (km/s)
A	1.22[a]	10.4	5.60	1.52	1.61	2.82	0.96	1.35	4.3	0.410	3.69
C	2.22[a]	21.0	6.0	1.58	1.68	4.63	1.58	4.7[b]	12.3	0.392	5.18
D	2.97[a]	30.0	6.12	1.52	1.65	5.30	2.01	4.0[b]	17.6	0.376	5.83
D	2.92[a]	29.4	6.72	1.57	1.67	5.35	1.95	4.7[b]	17.4	0.381	···
D	2.92[a]	29.4	6.77	1.72	1.71	5.45	1.93	3.8[c]	18.0	0.378	···
E	3.51[a]	36.5	5.94	1.51	1.63	5.55	2.33	4.7	21.1	0.356	4.05
F	8.34[d]	51.5	6.81	1.61	1.73	6.23	2.90	···	31.3	0.308	···
F	8.44[d]	53.8	···	···	1.77	6.45	2.99	···	34.1	0.303	···
G	8.47[d]	5.45	···	···	1.73	6.66	3.01	···	34.6	0.317	···
H	8.91[d]	65.7	···	···	1.73	7.02	3.46	···	41.9	0.294	···
I	9.19[d]	72.9	5.71	1.52	1.74	7.41	3.64	···	47.0	0.292	···
I	9.39[d]	78.3	···	···	1.73	7.47	3.84	···	49.5	0.281	···
J	5.04[e]	270	···	···	1.79	8.31	4.22	···	62.9	0.274	···
J	5.48[e]	307	···	···	1.78	8.72	4.58	···	71.0	0.267	···
J	6.07[e]	356	···	···	1.78	9.24	5.10	···	83.6	0.252	···
J	6.59[e]	405	···	···	1.79	9.83	5.42	···	95.4	0.251	···

[a]Free-surface velocity from inclined experiments.
[b]Film trace slope taken near apex (the rest was fuzzy).
[c]A 25-μm-Al foil was placed on prism to eliminate fuzzy response caused by a spray of light particles ahead of the main wave.
[d]Shock velocity in 2024 Al from flash-gap experiments.
[e]Ta projectile velocity from two-stage light-gas gun experiments.

TABLE V. Vitreous carbon summary.

Shock system	Base plate Free-surface, shock, or projectile velocity (km/s)	Pressure in standard (GPa)	Sound speed at 1 atm (km/s) C_L	C_s	Initial density ρ_0 (Mg/m^3)	Shock velocity U_s (km/s)	Particle velocity U_p (km/s)	Free-surface velocity U_{FS} (km/s)	Pressure P (GPa)	Volume V (m^3/Mg)	Sound speed at P C_* (km/s)
A[a]	0.78[b]	6.3	4.38	2.91	1.548	3.06[c]	0.56	0.92	2.8	0.53	···
A	1.21[b]	10.4	4.10	2.72	1.542	3.98[c]	0.87	1.62	5.4	0.519	···
C	2.15[b]	20.6	4.50	2.98	1.554	4.62	1.51	3.23	10.8	0.433	5.50
C	2.24[b]	21.1	4.11	2.73	1.546	4.65	1.55	3.14	11.1	0.431	···
D	3.03[b]	30.5	4.48	2.97	1.556	5.33	2.07	3.84	17.1	0.393	6.13
E	3.69[b]	39.8	4.43	2.84	1.547	5.97	2.16	4.53	22.7	0.380	6.74
F	8.44[d]	53.4	4.10	2.72	1.540	6.33	3.66	···	30.8	0.325	···
G	8.45[d]	54.0	4.11	2.73	1.539	6.41	3.11	···	30.7	0.335	···
H	8.89[d]	65.0	4.10	2.73	1.538	6.71	3.64	···	37.5	0.298	···
I	9.19[d]	72.9	4.10	2.74	1.535	7.08	3.84	···	41.8	0.297	···
J	5.56[e]	312	···	···	1.533	8.36	4.73	···	60.5	0.284	···
J	6.09[e]	356	···	···	1.536	8.93	5.16	···	70.7	0.275	···
J	6.84[e]	428	···	···	1.536	9.52	5.80	···	84.7	0.255	···

[a]With baratol instead of TNT.
[b]Free-surface velocity from inclined prisms.
[c]Two wave shock structures were observed. The Hugoniot elastic limits were about 0.6 GPa with $U_{s_1} = 4.22$ km/s and $U_{FS_1} = 0.2$ km/s and 1.8 GPa with $U_{s_1} = 4.27$ km/s and $U_{FS_1} = 0.54$ km/s, respectively.
[d]Shock velocity from flash-gap experiments.
[e]Ta projectile velocity from two-stage gas gun experiments.

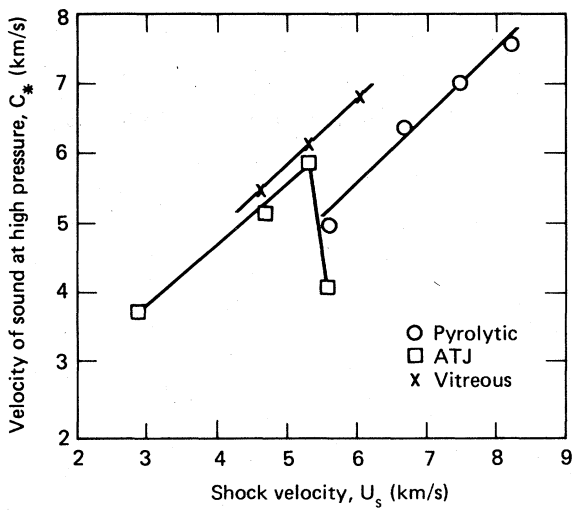

FIG. 4. Sound speed at pressures ranging from about 9.0 to 33 GPa vs shock velocity for pyrolytic graphite, ATJ graphite, and vitreous carbon. The curve for ATJ graphite exhibits a discontinuity that indicates a drastic decrease in C_* when in the mixed-phase regime (21.1 GPa). None of the materials exhibited the high velocities expected for carbon in the diamond phase.

synthetic graphite are given by $U_s = 2.85 + 2.52(U_p - 0.95)$ for $0.95 < U_p < 2.0$ km/s and $U_s = 5.55 + 1.39(U_p - 2.35)$ for $2.35 < U_p < 5.4$ km/s. The stresses corresponding to the discontinuities are 18 and 22 GPa. The large difference between $2U_p$ and U_{FS} was caused by a spray of particles that preceded the main free-surface wave.

The amorphous carbon exhibited a weak elastic wave, and the Hugoniot elastic limit was about 1.2 GPa. The three line segments (Fig. 3) are described by $U_s = 2.69 + 1.32U_p$ for $0 < U_p < 2.43$ km/s, $U_s = 5.96 + 0.63(U_p - 2.43)$ for $2.43 < U_p < 3.51$ km/s, and $U_s = 6.60 + 1.34(U_p - 3.51)$ for $3.51 < U_p < 6.0$ km/s. The stresses corresponding to the two discontinuities are 22.3 and 35.8 GPa.

In pyrolytic and amorphous carbon, the speed of sound at high pressure varied linearly with shock velocity (Fig. 4). For pyrolytic graphite, this was $C_* = 5.08 + 0.97(U_s - 5.50)$ for $5.50 < U_s < 8.10$ km/s. For vitreous carbon it was $C_* = 5.50 + 0.94(U_s - 4.62)$ for $4.62 < U_s < 5.30$ km/s. The relation for ATJ graphite was $C_* = 3.69 + 0.84(U_s - 2.82)$ for $2.82 < U_s < 5.30 <$ km/s. However in the mixed-phase region ($U_s < 5.30$ km/s) anomalous behavior was noted (see Fig. 4).

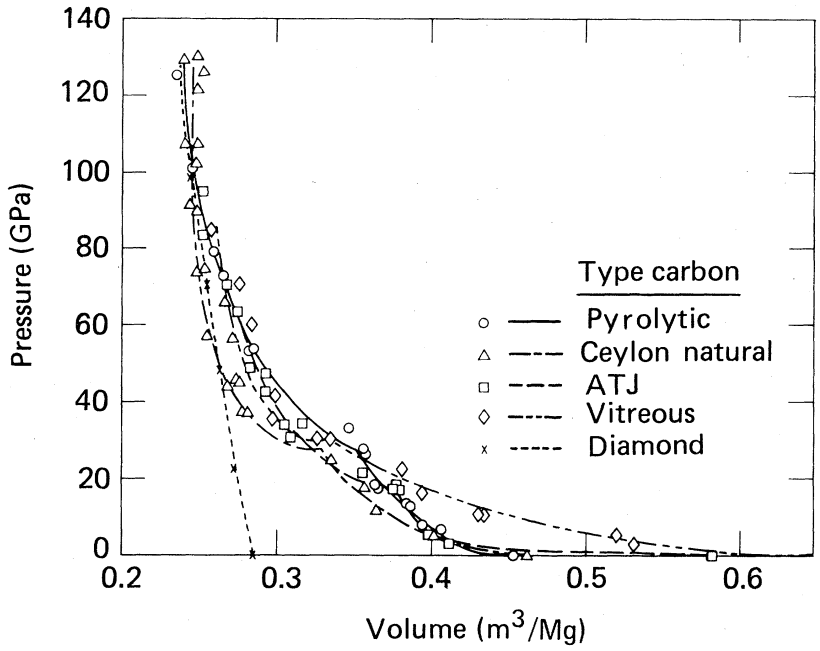

FIG. 5. Comparison of pressure vs volume curve for pyrolytic, Ceylon natural, and ATJ graphites and for amorphous carbon. The cusps are at the pressure points where the first discontinuity in the U_s vs U_p curve occurs. The diamond data are from Pavlovskii (Ref. 22).

V. DISCUSSION

The shock-velocity-versus-particle-velocity curves provide a sensitive means for locating response characteristics indicative of irregular behavior under compression. The slope of each plot is related to the derivative of the volume compressibility [Eq. (1)] and thus provides insight into material behavior under pressure.

The initial line segments of the curves for the three graphites are straight lines (Fig. 3), and usually there is excellent agreement with previously reported results. A regularly occurring density effect was noted, i.e., lower shock velocity for lower density.

Pyrolytic graphite data from Doran[13] and McQueen and Marsh[15] indicate a discontinuity at $U_p < 0.6$ km/s that we did not observe, but there was excellent agreement for the remainder of the graph. Our experiments were not done at as low a pressure as theirs. However, we used very sensitive prisms with a 921T Al base plate, so we could have observed multiple-wave structures; none were seen. Fowles[32] and Jones *et al.*[33] noted that 2024 Al exhibits a weak elastic precursor (~ 0.5 GPa), but 921T Al does not. It may be that the discontinuities noted elsewhere[13,15] were related to a catch-up interaction of the main shock with a weak elastic precursor that was initiated in the 2024 Al base plate these investigators used.

For all three graphites U_s vs U_p plots have discontinuities at $U_p \sim 1.5$ to 2.0 km/s (Fig. 3) that are considered to be manifestations of the onset of a solid-to-solid transition from the graphite to the diamond phase. The second line segments (the dashed horizontal portions) comprise mixed-phase regions and the discontinuities at about 1.3 to 2.0 km/s mark completion of the transition.

All three graphites also exhibit similar responses in the mixed-phase regions that are different from the response noted for the shock compression of highly oriented pyrolytic (graphitelike) boron nitride (BN).[28] For pyrolytic BN, U_s vs U_p had a slope of 1.02 in the mixed-phase, portion, thus indicating the possibility of a shock-induced transformation in BN to a metastable wurtzite[34] rather than the zinc-blende structure. Because no slope was observed in the mixed-phase region for graphite, it seems unlikely that there is a direct shock-induced transformation from graphite to wurtzite or hexagonal diamond at these pressures and temperatures.

All plots for values of U_p greater than that at the second discontinuity exhibit nearly equal slopes (the additional discontinuity in the Ceylon natural graphite curve will be discussed later). The change in compressibility is essentially the same for all three, and they probably have the same crystallographic structure (most likely cubic diamond). This is purely speculative; the slope for the wurtzite form is unknown.

Our cold pressed samples of Ceylon graphite had nearly the same density as a cold pressed type used

by McQueen and Marsh,[15] $\rho_0 \simeq 2.13$ Mg/m^3. Our data are in excellent agreement with that of McQueen and Marsh up to $U_p = 3.0$ km/s. Thereafter their slope is considerably steeper than ours (Fig. 3); however, one of our data points ($U_s = 8.49$, $U_p = 3.54$ km/s) was obtained with high explosive system I (Tables I and II) and fits their plot.

A graph of time versus distance for this high explosive experiment indicated that a reverberating rarefaction wave from the impactor probably overtook the initial shock inside the graphite sample and degraded the shock front. The amplitude for the particle velocity was thus reduced. In this analysis it was assumed that the speed of sound in each compressed material was $C_* = 1.3U_s$.

The material used by McQueen and Marsh[15] was of high purity. In a comparison of the two data sets, as far as the graphite-to-diamond transition is concerned, we see that the presence of a small amount of the known catalyst, Fe, in our samples had no effect; hence, it is concluded that significant catalytic nucleation did not occur on a microsecond time scale.

From $U_p = 2.6$ to 4.4 km/s our Ceylon graphite data from the two-stage light-gas gun plotted parallel to that for pyrolytic and ATJ graphites; thus the material appears to be in the diamond phase. The slope of U_s vs U_p for amorphous carbon (Fig. 3) has an initial line segment less than for the three graphites and indicates that the amorphous carbon is initially more compressible. The discontinuity at $U_p \simeq 2.4$ km/s is probably related to the onset of a phase transition, that at 3.5 km/s marks the completion. The positive slope for $2.4 < U_p < 3.5$ km/s may indicate a transition to the wurtzite form similar to that found for BN.[28,34] For $U_p > 3.25$ km/s, the slope is the same as for the three graphites, thus, indicating equal compressibility. Therefore, it appears that the structure at highest pressure is the same for all four materials, probably cubic diamond.

It is interesting that the amorphous form of carbon, which is a state of total crystallographic disorder, may be transformed to a state of order in microseconds through shock compression. Also, the trend for variation of shock velocity with density found for the graphites can apply to the transformed vitreous carbon.

The discontinuity in the Ceylon graphite plot at $U_p \cong 4.5$ km/s may indicate anomalous behavior, i.e., melting, transition from diamond to a metallic state, and shock-front degradation by an overtaking rarefaction wave from the 1.5-mm thick Ta flyer. Obviously the possibility of shock-front degradation must be eliminated before making any valid conclusions about the cause of an anomalous behavior.

For normal materials, the rarefaction wave propagates at about $C_* = C_0 V_0 / V$. For materials that change phase under compression, however, other estimates are used. One method proven to be realistic is simply $C_* = 1.3U_s$. We used this assumption for our analysis to obtain C_* for Ta and a slightly more restrictive method for the carbon. The data on shock compression for single-crystal diamond[22] indicate that at 200 GPa, $C_* = C_0 V_0 / V = 1.28C_0$; to be more stringent, we used $C_* = 1.5C_0 = 18.3$ km/s. A time-versus-distance graph utilizing these assumptions (Fig. 2) was plotted for each set of data of $U_p > 4.5$ km/s; no discontinuity resulted from the interaction of an overtaking rarefraction wave. Computer calculations with the KO code also excluded the possibility of a rarefraction-wave interaction. Thus, the discontinuity is probably related to a material property.

The Hugoniots for the pyrolytic and Ceylon graphites in a pressure-temperature plane are superimposed on combined theoretical[35] and experimental[8,36,37] phase diagrams (Fig. 6). Van Vechten's[35] predictions are based on scaling of volume changes in transitions of related groups IV and III–IV intermetallic compounds and on a simplified dielectric theory for internal energies. For carbon, this results in phase diagram in which a large portion of the diamond (α) phase lies adjacent to a liquid metal (β_1) phase. Van Vechten's theory predicts a diamond-to-metal transition with a diamond-metal-liquid triple point at about 118 GPa and 3080 K.

We attempted to use our shock-wave data directly to supplement the theoretical-experimental phase diagram (Fig. 6). Our model assumed thermodynamic equilibrium and $C_v = 3R$. The Grüneisen γ was obtained from a $\gamma(V)$ function, where linear segments representing the graphite and mixed and diamond phases were joined together (Fig. 7). The segments were normalized to the accepted values of γ for graphite and for diamond at normal densities. The Hugoniot, and C_V and γ, were used to compute the

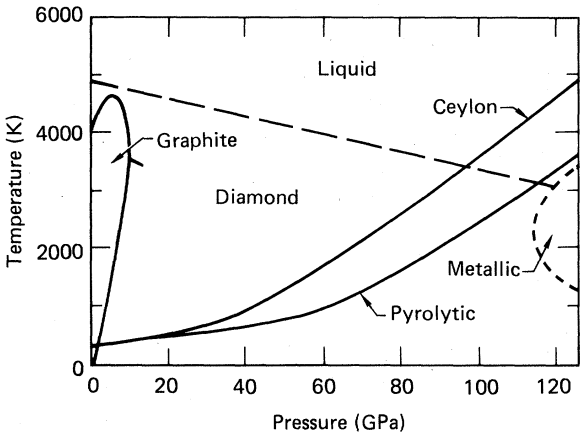

FIG. 6. Approximate Hugoniot calculations for pyrolytic and Ceylon graphite superimposed on theoretical (Ref. 35) and experimental (Refs. 8, 36, and 37) phase diagrams.

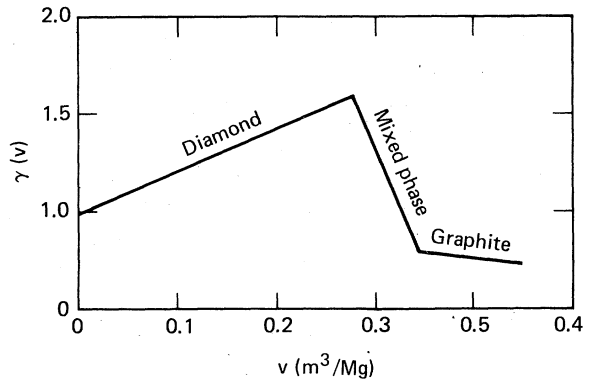

FIG. 7. The method used to approximate the Grüneisen gammas. The linear $\gamma(V)$ segments represent the graphite, mixed, and diamond phases. The segments were normalized to the accepted values of γ for graphite and for diamond at normal densities. The volumes at the discontinuities were obtained from the discontinuites in the corresponding U_s vs U_p curve (Fig. 3).

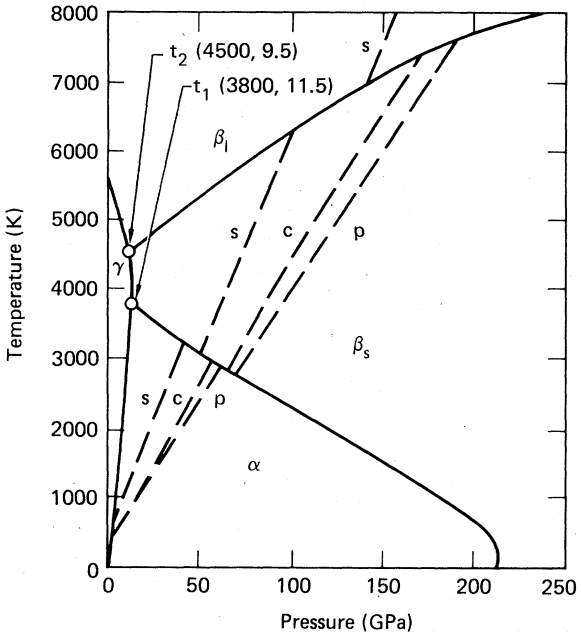

FIG. 8. Calculated Hugoniots for synthetic (s), Ceylon (c), and pyrolytic (p) graphite superimposed on the computed phase diagram Grover (Ref. 38) obtained when the volume change was assumed to be small. There is no direct transition path between the diamond and the liquid phases.

zero-degree isotherm and the Hugoniot temperatures from $P_H - P_0 = \gamma(V/V_0)(E_H - E_0)$.

The computed Hugoniot for pyrolytic graphite (Fig. 6) passes close to the theoretical diamond-metal-liquid triple point while that for Ceylon graphite crosses the melt curve at a lower pressure. In this model the kink in the U_s vs U_p curve for Ceylon graphite could repesent a shift from the diamond lattice to a more closely packed and less compressible metallic liquid. The maximum shock pressure for the less dense ATJ graphite was 95 GPa, while the pyrolytic graphite curve enters the liquid phase (if at all) at a pressure above 110 GPa. Thus, in neither of these cases would we expect to see the effects of melting as clearly as in the Hugoniots for Ceylon graphite.

A different theoretical approach has been used by Grover.[38] He noted that the diamond U_s vs U_p shock compression Hugoniot by Pavlovskii[22] does not extrapolate to bulk sound speed (C_B) at zero pressure. Therefore, he concluded that Pavlovskii's data are for an unknown very high-pressure phase. He predicted a diamond-to-metal transition at about 200 GPa and constructed a modified phase diagram using low-pressure ultrasonic compressibility data and known thermodynamic data for diamond. These data, and data derived through scaling known thermodynamic values from related elements, were combined with our very high-pressure Hugoniot results to study the expected diamond-to-metal phase transition.

Good graphite Hugoniot results were then obtained when a relatively lower density of the metallic phase was assumed in the computation. This technique produced a relatively low volume transformation (a few percent more dense than diamond) that ended in a solid metallic phase (Fig. 8). Grover assumed that the upper portions of the U_s-versus-U_p curve (Fig. 3) were in the β-metal phase. He interpreted the upper kink seen with the Ceylon graphite to be evidence of the melting of the β-metal phase and noted a pronounced effect resulting from the relatively large γ of the β phase and the large Hugoniot compression. Grover concluded that the model having a solid metallic phase (slightly more dense than diamond) in equilibrium with the diamond phase was the one most favored by experimental data and theory.

Grover also reported pressure versus temperature along a Hugoniot trajectroy corresponding to a transition from a diamond to a metal phase of the Van Vechten type. This calculation results in a 20% volume change, a large temperature drop, and a large U_s-U_p discontinuity as seen at the Hugoniot transition in Fig. 9. The difference in the magnitude of the estimated temperatures along the Hugoniots (Figs. 6 and 9) probably is a consequence related to the assumed specific heats, i.e., a Dulong-Petit value of $3R$ versus the Debye specific heat used by Grover. Use of the latter would move the transition boundary crossings to lower pressure (Figs. 8 and 9).

The phase diagram[39–41] for the related group IV element tin (Fig. 10) is similar to that shown in Fig.

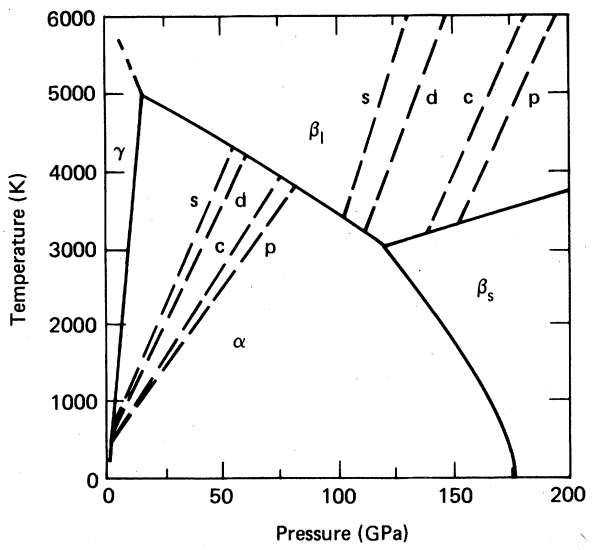

FIG. 9. Calculated Hugoniots for synthetic (s), Ceylon (c), and pyrolytic (p) graphites and porous diamond (d) superimposed upon Grover's (Ref. 38) computed phase diagram using the Van Vechten-type transition. The computed α-β_1 transition path shows a large volume change and a large temperature drop.

8. Tin exhibits a pressure-induced solid-to-solid transformation from the cubic (diamond α) to a tetragonal (β) form at temperatures less than melting. This α-to-β transition has $\sim 15\%$ change in volume unlike Grover's α-to-β transition. The slope of the melt line is positive with pressure. There is no direct transition path from the diamond to the liquid at positive pressures as there is for Si (Refs. 4, 5, 42, 43) and for Ge, (Refs. 4, 43, 44) other related elements. However, recovered samples of Si compressed above 10 GPa exhibited a complex cubic form with 16 atoms per unit cell[42] rather than the expected tetragonal form. In adddition, shock-wave experiments[6] with Si show multiple phase transitions in the 10- to 20-GPa region (their precise nature is unknown) that may indicate a phase diagram for Si resembling Sn. The situation for Ge is also somewhat obscure. The cubic tetragonal phase boundary and the melting curve were determined to 20 GPa,[43] but quenching experiments[44] yielded some uncertainty about new phases.

The proposed high-pressure phase diagrams for carbon (Figs. 7 to 9) are all speculative, but they point out areas where future research may be very productive. For example, measuring the Hugoniot elastic limit for diamond and determining the slope of the U_s vs U_p relation at low pressure would be very worthwhile (only low-pressure single-wave analysis on sintered diamond[23] has been done). The determination of the Hugoniot elastic limit would also help us understand the compressive characteristics of diamond anvils used in static pressure work.[45]

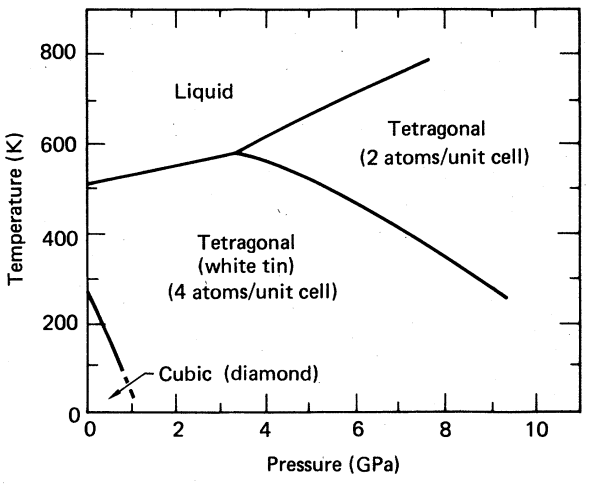

FIG. 10. Phase diagram for tin. It resembles Grover's computed Hugoniots for the graphites (Fig. 8).

VI. SUMMARY

We determined shock-compression parameters for three graphites to pressures about 50% higher than previously attained. Our low-pressure data, including the parameters describing the graphite-to-diamond phase transformation, are in good agreement with other work.[13–15] We also found evidence that indicates the pressure-induced diamond phase of carbon undergoes an additional transformation at very high pressure and temperature (74 GPa and 3000 K for Ceylon graphite).

All plots of U_s vs U_p were linear within each phase regime, i.e., graphite, diamond, and metallic. Discontinuities in the plots were taken to be manifestations of the points where material behavior under shock compression first occurred. No multiple-wave shock structures were observed for the graphites. The data for vitreous carbon indicate that it transforms from a disordered (glassy) state to an ordered (probably diamond) state under shock compression.

We used our shock-wave data at very high pressure to compare carbon phase diagrams obtained through use of Van Vechten's[35] and Grover's[38] theoretical models. At his time we concur with Grover's assertion that a low-volume, solid cubic diamond to solid tetragonal transition agrees best with the available experimental data.

ACKNOWLEDGMENTS

We wish to thank M. A. Benapfl, D. E. Bakker, R. E. Neatherland, and W. J. Nellis for technical assistance and R. W. Brown, A. Donnici, and L. F. Simmons for aid at the high-explosive test site. We are particularly grateful to B. L. Hord for the use of his unpublished Ceylon graphite data and to R. Grover and D. A. Young for helpful comments. This work was performed under the auspices of the U.S. Department of Energy by Lawrence Livermore National Laboratory under Contract No. W-7405-Eng-48.

---

[1]For a preliminary report on this work see W. H. Gust and D. A. Young, *High Pressure Science and Technology* (Plenum, New York, 1979), Vol. 1, p. 944.
[2]P. S. DeCarli and J. C. Jamieson, Science 133, 1821 (1961).
[3]B. J. Alder and R. H. Christian, Phys. Rev. Lett. 7, 367 (1961).
[4]S. Minomura and H. G. Drickamer, J. Phys. Chem. Solids 23, 451 (1962).
[5]J. C. Jamieson, Science 139, 764 (1963).
[6]W. H. Gust and E. B. Royce, J. Appl. Phys. 42, 1897 (1971).
[7]W. H. Gust and E. B. Royce, J. Appl. Phys. 43, 4437 (1972).
[8]F. P. Bundy, J. Chem. Phys. 38, 631 (1963).
[9]H. M. Strong, J. Chem. Phys. 39, 2057 (1963).
[10]F. P. Bundy and H. M. Strong, Solid State Phys. 13, 81 (1962).
[11]M. N. Pavlovskii and V. P. Drakin, Pis'ma Zh. Eksp. Teor. Fiz. 4, 169 (1966) [JETP Lett. 4, (1966)].
[12]R. F. Trunin, G. V. Simikov, B. N. Moiseev, L. F. Popov, and M. A. Podurets, Zh. Eksp. Teor. Fiz. 56, 1169 (1969) [Sov. Phys. JETP 29, 628 (1969)].
[13]D. G. Doran, J. Appl. Phys. 34, 844 (1964).
[14]N. L. Coleburn, J. Chem. Phys. 40, 71 (1964).
[15]R. G. McQueen and S. P. Marsh, *Symposium on High Dynamic Pressures, Paris, France, 1967* (Gordon and Breach, New York, 1968).
[16]L. F. Trueb, J. Appl. Phys. 39, 4707 (1968).
[17]L. F. Trueb, J. Appl. Phys. 42, 503 (1971).
[18]R. B. Aust and H. G. Drickamer, Science 140, 817 (1963).
[19]F. P. Bundy and J. S. Kasper, J. Chem. Phys. 46, 3437 (1967).
[20]R. E. Hanneman, H. M. Strong, and F. P. Bundy, Science 155, 995 (1967).
[21]L. F. Vereshchagin, E. N. Yakovlev, B. V. Vinogradov, V. P. Sakun, and G. N. Stepanov, High Temp.-High Pressures 6, 505 (1974).
[22]M. N. Pavlovskii, Fiz. Tverd. Tela. (Lenningrad) 13, 893 (1971) [Sov. Phys. Solid State 13, 741 (1971)].
[23]F. Smith, J. Fluid Mech. 17, 113 (1963).
[24]R. G. McQueen, S. P. Marsh, J. W. Taylor, J. N. Fritz, and W. J. Carter, in *High Velocity Impact Phenomena,* edited by Ray Kinslow (Academic, New York, 1970), pp. 312 and 320.
[25]J. J. Folkins and W. H. Gust, Bull. Am. Phys. Soc. 20, 1514 (1975).
[26]H. J. McSkimin and P. Andreatch, Jr., J. Appl. Phys. 43, 2944 (1972).
[27]Reference to a company or product name does not imply approval or recommendation of the product by the University of California or the U.S. Department of Energy to the exclusion of others that might be suitable.
[28]W. H. Gust and D. A. Young, Phys. Rev. B 15, 5012 (1977).
[29]Q. C. Johnson (private communication).
[30]F. C. Cowlard and J. C. Lewis, J. Mater. Sci. 2, 507 (1967).
[31]B. L. Hord (private communication).
[32]G. R. Fowles, J. Appl. Phys. 32, 1475 (1961).
[33]O. E. Jones, F. W. Nielson, and W. B. Benedick, J. Appl. Phys. 33, 3224 (1962).
[34]F. R. Corrigan and F. P. Bundy, J. Chem. Phys. 63, 3812 (1975).
[35]J. A. Van Vechten, Phys. Rev. B 7, 1479 (1973).
[36]N. S. Fateeva and L. F. Vereschagin, Pis'ma Zh. Eksp. Teor. Fiz. 13, 157 (1971) [JETP Lett. 13, 110 (1971)].
[37]G. R. Gathers, J. W. Shaner, and D. A. Young, Lawrence Livermore Laboratory Report No. UCRL-51644 (unpublished).
[38]R. Grover, J. Chem. Phys. 71, 3824 (1979).
[39]I. N. Nikolaev, N. P. Mar'in, V. N. Panyushkin, and L. S. Pavlykov, Fiz. Tverd. Tela. (Leningrad) 14, 2337 (1972) [Sov. Phys. Solid State 14, 2022 (1972)].
[40]A. Jayaraman, W. Klement, Jr., and G. C. Kennedy, Phys. Rev. 130, 540 (1963).
[41]T. D. Barnett, V. E. Bean, and H. T. Hall, J. Appl. Phys. 37, 875 (1965).
[42]R. H. Wentorf, Jr., and J. S. Kaspar, Science 139, 338 (1963).
[43]F. P. Bundy, J. Chem. Phys. 41, 3809 (1964).
[44]C. H. Bates, F. Dachille, and R. Roy, Science 147, 860 (1965).
[45]A. L. Ruoff, *High Pressure Science and Technology* (Plenum, New York, 1979), Vol. 2, p. 544.